OPEN ACCESS



Deviation from a Continuous and Universal Turbulence Cascade in NGC 6334 due to Massive Star Formation Activity

Junhao Liu (刘峻豪)¹, Qizhou Zhang², Hauyu Baobab Liu^{3,4}, Keping Qiu^{5,6}, Shanghuo Li⁷, Zhi-Yun Li⁸, Paul T. P. Ho^{1,4}, Josep Miquel Girart^{9,10}, Tao-Chung Ching¹¹, Huei-Ru Vivien Chen⁴, Shih-Ping Lai^{4,12}, Ramprasad Rao^{2,4}, and Ya-wen Tang⁴, and Ya-wen Tang⁴, Lest Asian Observatory, 660 N. A'ohōkū Place, University Park, Hilo, HI 96720, USA; liujunhao42@outlook.com, j.liu@eaobservatory.org

² Center for Astrophysics | Harvard & Smithsonian, 60 Garden Street, Cambridge, MA 02138, USA

³ Physics Department, National Sun Yat-Sen University, No. 70, Lien-Hai Road, Kaohsiung City 80424, Taiwan, Republic of China

⁴ Institute of Astronomy and Astrophysics, Academia Sinica, 11F of Astronomy-Mathematics Building, AS/NTU No.1, Sec. 4, Roosevelt Road, Taipei 10617,

Taiwan, Republic of China

⁵ School of Astronomy and Space Science, Nanjing University, 163 Xianlin Avenue, Nanjing 210023, Jiangsu, People's Republic of China

⁶ Key Laboratory of Modern Astronomy and Astrophysics (Nanjing University), Ministry of Education, Nanjing 210023, Jiangsu, People's Republic of China

⁷ Max Planck Institute for Astronomy, Konigstuhl 17, D-69117 Heidelberg, Germany

⁸ Astronomy Department, University of Virginia, Charlottesville, VA 22904-4325, USA

⁹ Institut de Ciències de l'Espai (ICE, CSIC), Can Magrans s/n, E-08193 Cerdanyola del Vallès, Catalonia, Spain

¹⁰ Institut d'Estudis Espacials de de Catalunya (IEEC), E-08034 Barcelona, Catalonia, Spain

¹¹ National Radio Astronomy Observatory, P.O. Box O, Socorro, NM 87801, USA

¹² Institute of Astronomy and Department of Physics, National Tsing Hua University, Hsinchu 30013, Taiwan, Republic of China

**Received 2022 December 22; revised 2023 March 14; accepted 2023 March 14; published 2023 May 24

Abstract

We use molecular line data from the Atacama Large Millimeter/submillimeter Array, Submillimeter Array, James Clerk Maxwell Telescope, and NANTEN2 to study the multiscale (\sim 15–0.005 pc) velocity statistics in the massive star formation region NGC 6334. We find that the nonthermal motions revealed by the velocity dispersion function (VDF) stay supersonic over scales of several orders of magnitude. The multiscale nonthermal motions revealed by different instruments do not follow the same continuous power law, which is because the massive star formation activities near central young stellar objects have increased the nonthermal motions in small-scale and high-density regions. The magnitudes of VDFs vary in different gas materials at the same scale, where the infrared dark clump N6334S in an early evolutionary stage shows a lower level of nonthermal motions than other more evolved clumps due to its more quiescent star formation activity. We find possible signs of small-scale-driven (e.g., by gravitational accretion or outflows) supersonic turbulence in clump N6334IV with a three-point VDF analysis. Our results clearly show that the scaling relation of velocity fields in NGC 6334 deviates from a continuous and universal turbulence cascade due to massive star formation activities.

Unified Astronomy Thesaurus concepts: Star formation (1569); Molecular clouds (1072); Interstellar medium (847)

1. Introduction

Turbulence plays an important role in the star formation process within molecular clouds 13 by providing support against gravitational collapse and regulating the hierarchical fragmentation of cloud substructures (Mac Low & Klessen 2004). One important property of turbulence is the relation of velocity statistics at different spatial scales. Since the first attempt by Larson (1981), scaling of the velocity structure has been extensively studied with the line width–size relation from molecular line observations. At > 0.1 pc scales, observational studies usually found a power-law scaling for the line width–size relation (e.g., Myers 1983; Solomon et al. 1987; Caselli & Myers 1995), which was interpreted as a natural consequence of turbulence cascade. At < 0.1 pc scales, the line width–size relation could transit to "coherent" (i.e., constant line width) for low-mass dense cores due to the dominance of thermal motions

Original content from this work may be used under the terms of the Creative Commons Attribution 4.0 licence. Any further distribution of this work must maintain attribution to the author(s) and the title of the work, journal citation and DOI.

over nonthermal motions (Goodman et al. 1998), but the relation in a high-mass star formation region is less clear due to rarer observations.

Other than the line width–size relation, the dispersion function (autocorrelation function or structure function) of velocity centroids can also be used to study the scaling relation of velocity fields in molecular clouds (e.g., Dickman & Kleiner 1985; Miesch & Bally 1994). Compared to the line width, the velocity centroid is advantageous in revealing the nonthermal motions because it is not sensitive to thermal broadening (Lazarian et al. 2022). The velocity centroid also does not suffer from the effect of line-of-sight signal integration that could broaden the observed line width (Cho & Yoo 2016). However, the dispersion function of velocity centroids is relatively less applied to observations due to its complexity.

NGC 6334 is a nearby (~1.3 kpc; Chibueze et al. 2014; Wu et al. 2014) massive star formation region. Six massive clumps (N6334I-V and N6334I(N)) with active massive star formation activities were identified in the predominant 10 pc long NGC 6334 filament located at the center of the NGC 6334 region with far-infrared/submillimeter/millimeter observations (e.g., Cheung et al. 1978; McBreen et al. 1979; Gezari 1982). In addition, a massive infrared dark clump N6334S is located near the southwestern end of the NGC 6334 region. In this paper,

 $[\]overline{^{13}}$ The nomenclature of cloud (\sim 10 pc), clump (\sim 1 pc), core (\sim 0.1 pc), and condensation (\sim 0.01 pc) scales in this paper follows Zhang et al. (2009).

Table 1Summary of Molecular Line Data

Line	Frequency (GHz)	E _u /k ^a (K)	n _c ^b (cm ⁻³)	Instrument	l _{beam} c (")	l _{MRS} ^d (")	Targets
OCS (19–18)	231.0610	110.9	4.8×10^{5}	ALMA	0.7	13	I(N), I, IV, V
¹³ CS (5–4)	231.2207	33.3	5.4×10^{6}	ALMA	0.7	13	I(N), I, IV, V
$H^{13}CO^{+}$ (1–0)	86.7543	4.2	1.8×10^{5}	ALMA	4.1	30	S
$NH_2D (1_{1,1}-1_{0,1})$	85.9263	20.7	6.5×10^{4}	ALMA	4.1	30	S
$H^{13}CO^{+}$ (4–3)	346.9983	41.6	9.2×10^{6}	SMA	4	20	I(N), I, IV, V
¹³ CO (3–2)	330.5880	31.7	3.1×10^{4}	JCMT	14	•••	I(N), I
¹² CO (1–0)	115.2712	5.5	2.2×10^{3}	NANTEN2	180		Cloud

Notes. The line information is from the CDMS (Muller et al. 2001) and LAMDA (Schöier et al. 2005) databases.

we present a multiscale study of the velocity statistics in five massive clumps (N6334I(N), I, IV, V, and S) as well as their parental structures in NGC 6334 using velocity centroid structure functions of different molecular line tracers from different instruments.

2. Observation

A particular line tracer is insensitive to gas below its critical density and is only sensitive to densities at most a factor of 2 orders of magnitude above its critical density (Goodman et al. 1998), so we use different line tracers to trace gas materials at different densities. The information of the molecular line data is summarized in Table 1. The critical density (n_c) of each line is estimated with $n_c = A_{\rm ul}/q_{\rm ul}(T)$, where $A_{\rm ul}$, $q_{\rm ul}(T)$, and T are the Einstein coefficient, collision rate coefficient, and gas temperature, respectively. Values of $A_{\rm ul}$ and $q_{\rm ul}$ are adopted from the CDMS (Muller et al. 2001) and LAMDA (Schöier et al. 2005) databases. No information on the collision rate coefficient exists for 13 CS and 13 CO $^+$ in LAMDA, so we adopt the values for CS and HCO $^+$ instead. Detailed observational parameters for each line can be found in the subsections below.

2.1. ALMA Observation

We carried out ALMA Band 6 dust continuum and molecular line observations toward four clumps (N6334I(N), I, IV, and V) in the massive region NGC 6334 in C43-1 and C43-4 configurations under the project 2017.1.00793.S (PI: Qizhou Zhang). Part of the data was reported in Liu et al. (2023). We adopt the OCS (19–18) and 13 CS (5–4) line data from the ALMA observations. The spatial resolution (l_{beam}) of the combined (C43-1 and C43-4) images is ~ 0.77 (~ 0.004 pc at a distance of 1.3 kpc). The maximum recoverable scale¹⁴ $(l_{\rm MRS})$ is $\sim 13''$ (~ 0.08 pc). The rms noises of the spectral line cubes with a velocity channel width of 0.16 km s⁻¹ are \sim 3.8, 8.7, 3.0, and 5.2 mJy beam $^{-1}$ for N6334I(N), I, IV, and V, respectively. More details on the ALMA data can be found in Liu et al. (2023). The high critical densities of OCS (19–18) and ¹³CS (5–4) make them suitable for studying the kinematics in the molecular dense cores/condensations in N6334I(N), I, IV, and V $(n \sim 10^7 - 10^9 \text{ cm}^{-3})$; Sadaghiani et al. 2020;

Palau et al. 2021) except for the highest density fragments. The high upper energy level (E_u/k) of OCS (19–18) makes it sensitive to the hot gas within those dense structures, while ¹³CS (5–4) could trace colder materials due to its relatively lower E_u/k .

We adopt the $\mathrm{H}^{13}\mathrm{CO}^{+}$ (1–0) and $\mathrm{NH}_2\mathrm{D}$ (1_{1,1}–1_{0,1}) line data (ID: 2016.1.00951.S; PI: Shaye Strom) from Li et al. (2020) and Li et al. (2022). The spatial and spectral resolutions are \sim 4."1 (\sim 0.026 pc) and 0.21 km s⁻¹, respectively. The maximum recoverable scale is \sim 30" (\sim 0.19 pc). The rms noise level is 6 mJy beam⁻¹ per channel. The high critical densities of $\mathrm{H}^{13}\mathrm{CO}^{+}$ (1–0) and $\mathrm{NH}_2\mathrm{D}$ (1_{1,1}–1_{0,1}) make them suitable for studying the kinematics in the molecular dense cores in N6334S ($n \sim 10^5$ –108 cm⁻³; Li et al. 2020) except for the highest density fragments. The E_u/k of the two lines is not far from the temperature of N6334S (\sim 15 K; Li et al. 2020).

2.2. SMA Data

We adopt the $\mathrm{H}^{13}\mathrm{CO}^{+}$ (5–4) line data of N6334I(N), I, IV, and V from the Submillimeter Array (SMA) observations that were reported in Zhang et al. (2014) and Palau et al. (2021). The spatial resolution is \sim 4" (\sim 0.025 pc) for N6334V and \sim 2" (\sim 0.013 pc) for the other clumps. The maximum recoverable scale is \sim 20" (\sim 0.13 pc), as reported by Zhang et al. (2014). The spectral resolution is 0.7 km s⁻¹. The rms noise of the 0.7 km s⁻¹ interval line cubes is \sim 0.2 Jy beam⁻¹. The high critical density of $\mathrm{H}^{13}\mathrm{CO}^{+}$ (5–4) makes it suitable for studying the kinematics in molecular dense cores/condensations in N6334I (N), I, IV, and V ($n \sim 10^7 - 10^9$ cm⁻³; Sadaghiani et al. 2020; Palau et al. 2021), but its relatively low E_{u}/k makes it less sensitive to hot gas materials.

2.3. JCMT Data

We include in our analysis the 13 CO (3–2) line cubes toward N6334I(N) and N6334I taken with the Heterodyne Array Receiver Program (HARP) and Auto-Correlation Spectrometer and Imaging System (ACSIS; Buckle et al. 2009) from the JCMT data archive (program code: M11BN07). The 13 CO (3–2) data have been previously reported in Liu et al. (2023). The spatial and spectral resolutions of the 13 CO (3–2) data are $\sim 14''$ (~ 0.09 pc) and 0.055 km s $^{-1}$, respectively. The map size is $2' \times 2'$ ($\sim 0.76 \times 0.76$ pc) for each field. The rms noises of N6334I(N) and N6334I are 1.2 and 0.6 K per channel,

^a Upper energy level in kelvin.

^b Critical density at specific temperatures (see Section 3.3). For 13 CS and H^{13} CO $^+$, we adopt the collision rate coefficient of the main isotope. For ALMA OCS (19–18) and 13 CS (5–4) and SMA H^{13} CO $^+$ (4–3) lines, we adopt $T_{gas} \sim 100$ K in the calculation of n_c .

^c Size of the beam for the single-dish or major size of the synthesized beam for the interferometer.

d Maximum recoverable scale for interferometers.

¹⁴ https://almascience.eso.org/observing/observing-configuration-schedule/prior-cycle-observing-and-configuration-schedule

respectively, in antenna radiation temperature ($T_{\rm R}^*$). The critical density of ¹³CO (3–2) is suitable for studying the kinematics in the northern hub (covering N6334I(N) and I) of the NGC 6334 cloud ($n \sim$ several times of 10^5 cm⁻³; André et al. 2016; Sadaghiani et al. 2020; Arzoumanian et al. 2021).

2.4. NANTEN2 Data

We also include in our analysis the NANTEN2 12 CO (1–0) data from Fukui et al. (2018). The spatial and spectral resolutions of the 12 CO (1–0) cubes are \sim 3′ (\sim 1.1 pc) and 0.16 km s $^{-1}$, respectively. The typical rms noise level is \sim 1.2 K per channel. The appropriate critical density of 12 CO (1–0) makes it suitable for studying the kinematics of the NGC 6334 cloud and its surrounding material in the same complex ($n \sim 3.2 \times 10^3$ cm $^{-3}$; Kraemer & Jackson 1999).

3. Results

3.1. Molecular Lines and Velocity Centroids

We use NANTEN2 12 CO (1–0), JCMT 13 CO (3–2), SMA H 13 CO $^+$ (5–4), and ALMA H 13 CO $^+$ (1–0), NH $_2$ D (1 $_{1,1}$ –1 $_{0,1}$), OCS (19–18), and 13 CS (5–4) line data to reveal the kinematics in NGC 6334 at different densities and scales. We estimate the velocity centroid $V_c(x)$ at position x with

$$V_c(\mathbf{x}) = \frac{\sum_{i}^{N_{\text{ch}}} I_i(\mathbf{x}) v_i \Delta v_{\text{ch}}}{\sum_{i}^{N_{\text{ch}}} I_i(\mathbf{x}) \Delta v_{\text{ch}}},$$
(1)

where $I_i(\mathbf{x})$, v_i , $\Delta v_{\rm ch}$, and $N_{\rm ch}$ are the line intensity, line-of-sight velocity, channel width, and number of integrated channels, respectively. The multiscale intensity-weighted velocity centroid (i.e., moment 1) maps are shown in the Appendix. For the NANTEN2 and JCMT observations, we only consider the line emission from -12 to 4 km s⁻¹, which covers the main velocity component at these scales (Fukui et al. 2018; Arzoumanian et al. 2022). For the SMA and ALMA observations, we only consider velocities within \sim 5 km s⁻¹ (\sim 4 km s⁻¹ for N6334S to be consistent with Li et al. 2020) with respect to the local-standard-of-rest (LSR) velocity of the clump to avoid the contamination from outflows (Liu et al. 2022c). The LSR velocities are $\sim -3.5, -7.5, -3.5, \text{ and } -6$ km s⁻¹ for N6334I(N), I, IV, and V, respectively, rounded to the nearest 0.5 decimal (Liu et al. 2022c). Ordered velocity gradients in NGC 6334 have previously been reported across different spatial scales (Juárez et al. 2017; Fukui et al. 2018; Arzoumanian et al. 2022; Liu 2023).

3.2. Velocity Centroid Dispersion Functions

3.2.1. Two-point Velocity Centroid Dispersion Functions

We use the velocity dispersion function (VDF) in the form of structure functions of velocity centroids to characterize the multiscale velocity fields in NGC 6334. We calculate the conventionally two-point VDFs at different distance intervals (*l*) as

$$\langle \Delta V_c^2(\boldsymbol{l}) \rangle^{\frac{1}{2}} = \langle (V_c(\boldsymbol{x} + \boldsymbol{l}) - V_c(\boldsymbol{x}))^2 \rangle_{\bar{x}}^{\frac{1}{2}}.$$
 (2)

The data are divided into separate distance bins with sizes corresponding to half of the beam size. For the NANTEN2 data, we only consider the area with NANTEN2 integrated

¹²CO (1–0) intensity greater than 25 K km s⁻¹, which approximately corresponds to the area of the NGC 6334 complex (Fukui et al. 2018). We consider the whole mapping area for the JCMT data. For the SMA and ALMA data, we only consider regions with SNR > 3 for both the dust continuum and integrated line intensity (moment 0) maps (not shown in this paper). Because the small-scale statistics could be affected by the beam-smoothing effect (Miesch & Bally 1994), we only consider data points with $l \gtrsim l_{\rm beam}$. Because the large-scale statistics could be affected by the sparse sampling effect (Liu et al. 2022b), we only consider data points with distance intervals smaller than the effective radius $R_{\rm eff} = \sqrt{A/\pi}$, where A is the area of each considered region. Moreover, because of the large number of data points included in each distance bin, the statistical errors for the VDFs are negligible (Miesch & Bally 1994). Thus, we do not present error bars for the VDFs.

The upper left panel of Figure 1 shows the VDFs for different lines, while the upper right panel presents a zoomed-in image of the VDFs at small scales. All the VDFs show positive slopes. Similar to the angular dispersion function (ADF) of polarization position angles (see Figure 1 of Hildebrand et al. 2009), the positive slopes of the VDFs are natural results of a combination of local turbulent and ordered velocity fields. The VDF of N6334I(N) at clump-to-core scales (\sim 1–0.1 pc) revealed by JCMT ¹³CO (3–2) observations seems to roughly follow the same power law as the VDF at cloud-to-clump scales (\sim 10–1 pc) revealed by NANTEN2 ¹²CO (1–0) observations, which suggests that the nonthermal motions in N6334I(N) at clump-to-core scales mainly originate from the cascade of the cloud turbulence. With a simple least-square fit for the continuous power law of the JCMT VDF of N6334I(N) and the NANTEN2 VDF of the cloud, we obtain $\langle (\Delta V_c)^2 \rangle^{\frac{1}{2}} \sim l^{0.44}$ (see Figure 1). The power-law index of 0.44 is consistent with previous VDF studies (e.g., \sim 0.43; Miesch & Bally 1994). On the other hand, the JCMT VDF of N6334I at clump-to-core scales is clearly higher (by a factor of \sim 2) than the fitted power law, which suggests that the clumpto-core scale nonthermal motions in N6334I have been increased by massive star formation activities.

At subcore ($\lesssim 0.1$ pc) scales revealed by SMA and ALMA, the VDFs are comparable to or higher than the JCMT VDFs at clump-to-core scales and are much higher (up to a factor of \sim 20) than the fitted power law, suggesting that the nonthermal motions are significantly increased in small-scale high-density regions. For interferometric observations, the filtering of largescale emissions could be a source of uncertainty for the VDF analysis. There is a lack of studies on how the filtering effect could affect the VDFs. If the nonthermal motions are universal at different densities and the VDFs behave similarly to the ADFs, the filtering effect should only affect data points at scales close to $l_{\rm MRS}$ (Houde et al. 2016). Thus, the filtering effect might not significantly affect our SMA and ALMA VDFs except for the largest several *l* bins. This is because we only consider data points with l smaller than the effective radius and we have $R_{\rm eff} < l_{\rm MRS}$ for all the interferometer VDFs. However, due to the lack of theoretical studies, it is unclear whether the filtering effect should affect the VDFs and ADFs similarly. Also, it is expected that the nonthermal motions are more significant in higher-density regions at the same scale due to more active star formation activities. As interferometric observations filter out the diffuse emissions, the

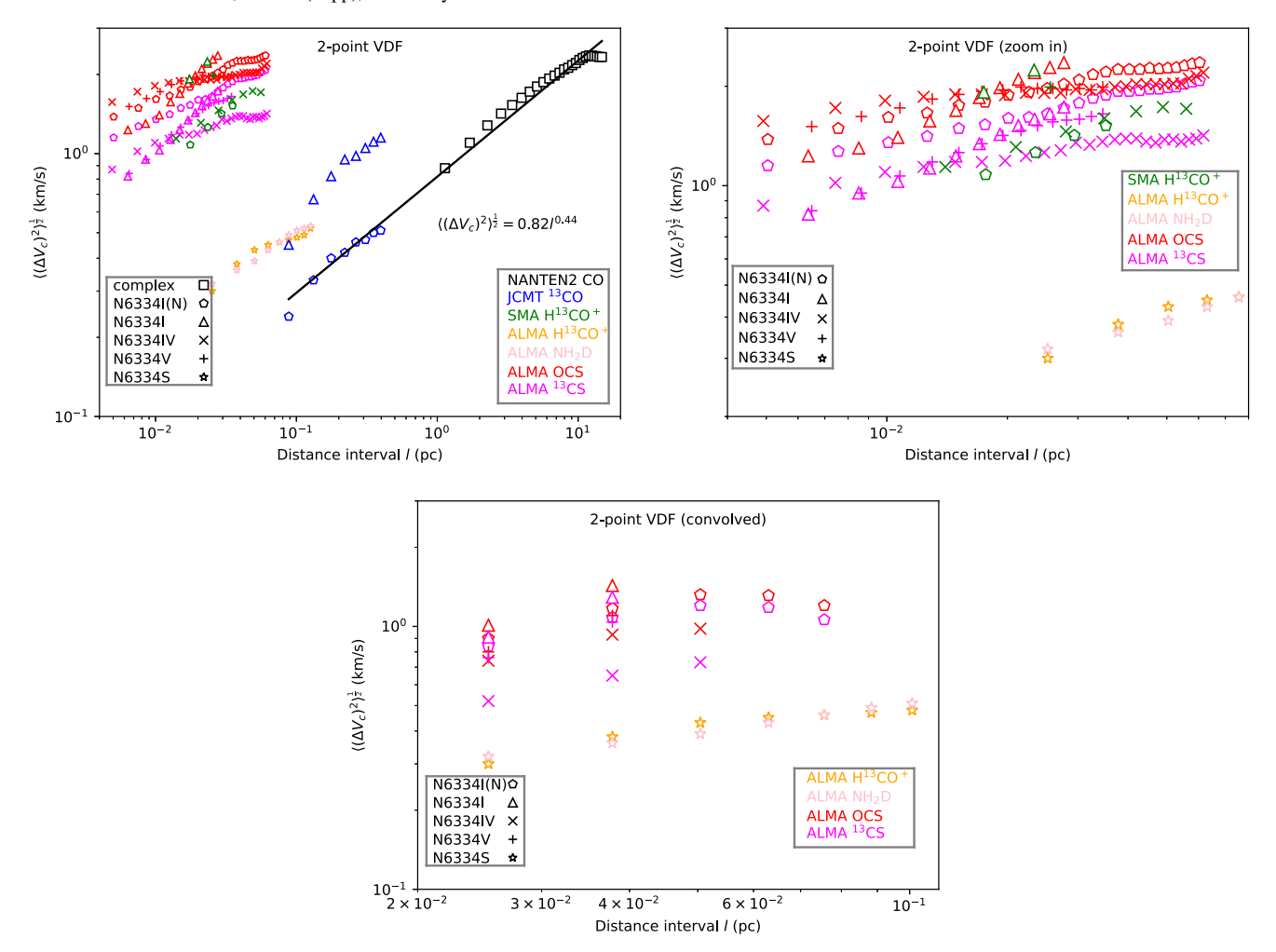


Figure 1. Upper left panel: two-point dispersion functions of velocity centroids. The solid black line presents the result of a simple power-law fit for the JCMT VDF of N6334I(N) and the NANTEN2 VDF of the cloud. Upper right panel: a zoomed-in image of the upper left panel at small scales. Lower panel: convolved ALMA two-point dispersion functions of velocity centroids. Different symbols represent different regions. Different colors indicate different instruments and lines. Only data points with *l* greater than the beam resolution and smaller than the effective radius of the considered region are shown.

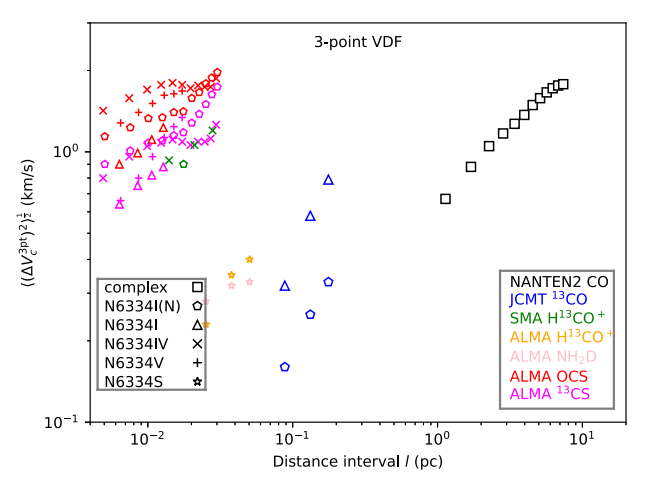
small-scale regions in diffuse gas materials with flat density profiles cannot be observed with interferometers. Thus, we cannot rule out the possibility that the velocity statistics in small-scale low-density regions still follow the large-scale turbulence cascade.

Other than the increase of VDFs in small-scale high-density regions, we also see that the VDFs from the same instrument and line but in different regions show different levels of amplitudes at the same scale. As discussed in Section 4 below, the increase of nonthermal motions in high-density regions could be related to massive star formation activities near young stellar objects (YSOs) such as infall, rotation, and/or H II regions. Small-scale outflow- or gravity-driven turbulence may also contribute to the increase of nonthermal motions. Thus, the varying evolutionary stages and star formation activities in different regions could naturally explain the different VDF amplitudes in different clumps.

On the other hand, the VDFs from different lines but of the same clump show different amplitudes in N6334I(N), I, IV, and V. For the ALMA line observations toward these clumps, the OCS VDFs are always higher than the 13 CS VDFs toward the same clump. This could possibly be explained by the higher $E_{\rm u}/k$ of the OCS (19–18) line; i.e., the OCS (19–18) line could trace hotter materials closer to the YSOs with more active star

formation activities. The variations in the optical depth and chemical history of the two lines could also contribute to the difference in the VDFs. Similar reasons, adding the difference in critical densities, beam resolution, filtering scale, and area of the considered region, might explain the inconsistency between the SMA $\rm H^{13}CO^{+}$ VDFs and the ALMA VDFs toward the same clumps. The situation is different in N6334S. Although the physical conditions traced by $\rm H^{13}CO^{+}$ (1–0) and NH₂D (1_{1,1}–1_{0,1}) are different (Li et al. 2020), the VDFs of the two lines are similar in shape and magnitude in N6334S. This may suggest that the nonthermal motions are coherent in different gas materials in N6334S due to the quiescent star formation activities.

To compare the ALMA VDFs in different clumps and reduce the influence of the different beam resolutions, we convolve the ALMA line data toward N6334I(N), I, IV, and V to a similar resolution to N6334S. The VDFs for the convolved ALMA data are shown in the lower panel of Figure 1. The ALMA H¹³CO⁺ and NH₂D VDFs toward the infrared dark clump N6334S are much lower than the convolved ALMA OCS and ¹³CS VDFs toward other more evolved clumps. Although this could be partially due to the difference in the filtering scale and line excitation condition, we suggest that the active star formation activity in more evolved clumps may be



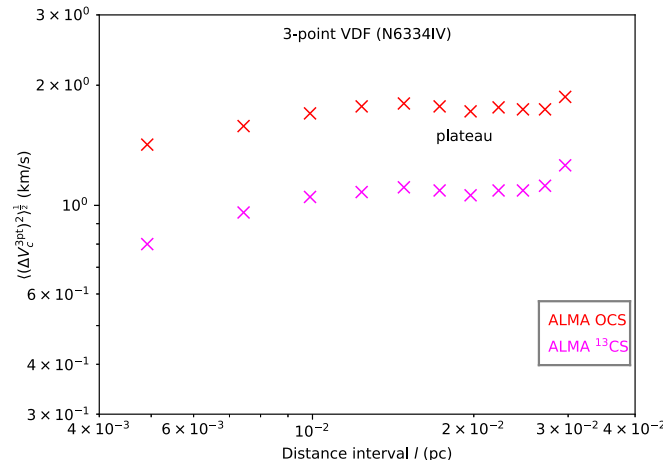


Figure 2. Left: three-point dispersion functions of velocity centroids. Right: same as left but only for the ALMA VDF of N6334IV. Different symbols represent different regions. Different colors indicate different instruments and lines. Only data points with *l* greater than the beam resolution and smaller than half of the effective radius of the considered region are shown.

the main reason for the observed higher VDFs in N6334I(N), I, IV, and V. Future observational studies with the same line tracers and observational parameters toward regions at different evolutionary stages are necessary to further confirm this.

3.2.2. Three-point Velocity Centroid Dispersion Functions

The ordered velocity gradients at different scales in NGC 6334 (see Appendix) make it difficult to derive pure turbulence statistics with the nonthermal VDFs. Lazarian et al. (2022) suggested that the ordered field contribution to the VDFs can be removed by calculating multipoint dispersion functions (Cho 2019) instead of the usually adopted two-point dispersion functions. The simplest three-point VDF is calculated as (Cho 2019)

$$\langle \Delta (V_c^{3\text{pt}})^2 (\boldsymbol{l}) \rangle^{\frac{1}{2}} = \langle (V_c(\boldsymbol{x} - \boldsymbol{l}) - 2V_c(\boldsymbol{x}) + V_c(\boldsymbol{x} + \boldsymbol{l}))^2 \rangle_x^{\frac{1}{2}} / \sqrt{3}. \quad (3)$$

It is easily understood that the three-point VDF can exactly remove a constant velocity gradient by averaging negative and positive gradients at distance l. Similarly, an n-point VDF can exactly remove a large-scale $V_c(x)$ in the form of a polynomial of degree n-2 (Cho 2019). Thus, multipoint dispersion functions can remove complex ordered fields by treating the ordered fields as high-order polynomials. Using simulated maps with small-scale fluctuations superimposed on large-scale variations, Cho (2019) demonstrated that the multipoint dispersion function can effectively remove the large-scale variations and leave only the small-scale turbulent fluctuations. More point dispersion functions can remove more complex ordered fields but will also increase the noise. If the ordered velocity field is successfully removed, the multipoint VDF should show a plateau corresponding to the level of the local turbulence (Cho 2019). It should be noted that the multipoint dispersion function could remove the low spatial frequency turbulence as well as the ordered velocity fields (Liu et al. 2022b).

Following Cho (2019), we calculate the three-point VDFs for the same molecular line data used for calculating the two-point VDFs. The left panel of Figure 2 shows the derived three-point VDFs. The three-point VDFs are lower and present larger scatters than the two-point VDFs, but the relation between

three-point VDFs for different lines and regions is similar to those of the two-point VDFs. On the other hand, except for the ALMA VDFs of N6334IV, which show a clear plateau (right panel of Figure 2), the three-point VDFs for most lines still show positive slopes without signs of plateau-like features. This is in agreement with the velocity centroid maps (Figure 7 in the Appendix) where N6334IV does not show clearly ordered velocity gradients. The positive slopes in other threepoint VDFs suggest that there are ordered velocity components remaining or that the upper l limit of the VDF is smaller than the l range of the plateau. Unfortunately, the size-to-resolution ratio of our data does not allow us to calculate more point dispersion functions to further remove the contribution from ordered velocity fields. It is unclear how the filtering effect of interferometers could affect the multipoint dispersion function analysis, which needs to be addressed by future theoretical and numerical studies.

3.3. Sonic Mach Number

We estimate the sonic Mach number for the nonthermal motions with the two-point VDFs. Similar to the relation between the ADF and the angular dispersion (Hildebrand et al. 2009), the VDF and the velocity centroid dispersion (δV_c) have the relation $\langle (\Delta V_c)^2 \rangle^{\frac{1}{2}} = \sqrt{2(\langle V_c^2 \rangle - \langle V_c \rangle^2)} = \sqrt{2} \, \delta V_c$. Assuming that δV_c is $1/\sqrt{3}$ times the 3D nonthermal velocity dispersion, we estimate the 3D sonic Mach number 15 with $\mathcal{M}_s = \sqrt{3} \langle (\Delta V_c)^2 \rangle^{\frac{1}{2}} / (\sqrt{2} c_s)$. The 1D sound speed for isothermal gas is estimated as $c_s = \sqrt{k_{\rm B}T/(\mu_{\rm p}m_{\rm H})}$, where $k_{\rm B}$ is the Boltzmann constant, T is the gas temperature, $\mu_{\rm p} = 2.37$ (Kauffmann et al. 2008) is the mean molecular weight per free particle, and $m_{\rm H}$ is the atomic mass of hydrogen. We adopt T = 20 K for NANTEN2 and JCMT observations because the temperature variation in NGC 6334 is small at these scales (Arzoumanian et al. 2021). We adopt T = 15 K for ALMA observations toward N6334S (Li et al. 2020). We do not calculate \mathcal{M}_s for the SMA observations due to the lack of temperature estimation. The average temperature of our considered regions in N6334I(N), I, IV, and V are ∼61, 167,

 $[\]overline{^{15}}$ Some previous studies report the 1D sonic Mach number, which is the ratio between the 1D nonthermal velocity dispersion and sound speed. There is a factor of $\sqrt{3}$ difference between the 1D and 3D sonic Mach number.

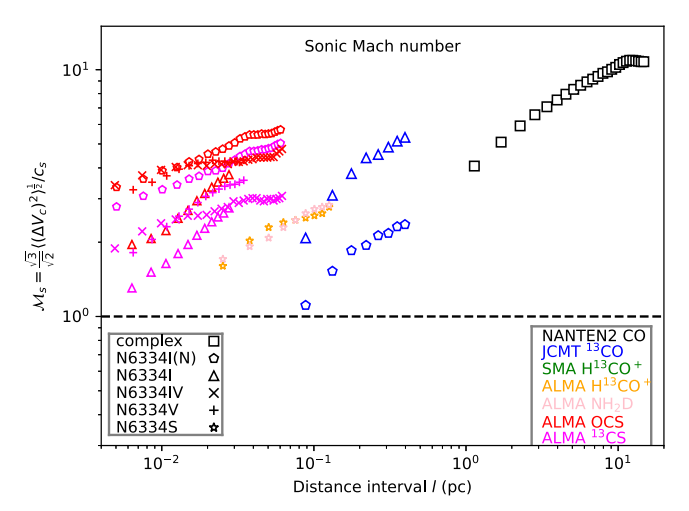


Figure 3. Sonic Mach number as a function of distance interval. Different symbols represent different regions. Different colors indicate different instruments and lines. Only data points with l greater than the beam resolution and smaller than the effective radius of the considered region are shown.

67, and 83 K, respectively, for the ALMA observations (Liu et al. 2023). Figure 3 shows the calculated \mathcal{M}_s at different scales. The derived \mathcal{M}_s ranges from ~ 11 to ~ 1.1 at ~ 15 –0.005 pc scales, which stays supersonic ¹⁶ (i.e., $\mathcal{M}_s > 1$) across 3–4 orders of magnitude. We also estimated the \mathcal{M}_s for the small-scale turbulent motions in N6334IV with the three-point ALMA VDFs, which stays supersonic as well.

4. Discussion

4.1. Nonthermal Motions in Massive Star Formation Regions

Nonthermal motions can be divided into nonturbulent (ordered) and turbulent motions. If both the ordered and turbulent motions originate from the same turbulence cascade, the small-scale ordered motion is actually part of the turbulent motion at larger scales (Miesch & Bally 1994), and the velocity statistics for nonthermal motions should show a continuous power-law relation across different scales. However, except for the JCMT VDF of N6334I(N) and the NANTEN2 VDF of the cloud, the VDFs from different data sets at different scales are not continuous in general (see Figure 1). On the other hand, the VDFs from the same line toward different clumps and the VDFs from different lines toward the same clump show distinct magnitudes at the same scale, so the VDFs are not universal either. Thus, it is unlikely that the nonthermal motions in star formation regions in NGC 6334are solely due to the cascade of global supersonic turbulence in the interstellar medium (ISM). It should be noted that the multiscale nonthermal motions in low-density regions without star formation activities may still follow a continuous turbulence cascade. But such low-density regions are not the focus of this star formation study.

Alternatively, it is expected that the massive star formation activity near YSOs can increase the nonthermal motions in small-scale and high-density regions as the region evolves. Such effects have been previously observed in massive star formation regions (e.g., Zhang et al. 1998). The various star formation activities in different clumps can naturally explain the different magnitudes of VDFs at the same scale. Especially,

the ALMA VDFs in the infrared dark N6334S are much lower than the ALMA VDFs in more evolved clumps at the same scale, which confirms that the nonthermal motion is increased as the clump/core evolves. This trend is in agreement with previous line width observations in the infrared dark cloud G28.34 (Wang et al. 2008), in which the authors found that the large-scale line width is broader than the small-scale line width in an infrared dark clump (P1 or MM4) at an earlier evolution stage but is narrower than the small-scale line width in an infrared bright clump (P2 or MM1) that is more evolved. On the other hand, the ALMA VDFs for N6334S are comparable to or higher than the JCMT VDF toward N6334I(N) at a larger scale, which suggests the star formation activities have already increased the nonthermal motions in early stages of massive star formation in massive dense cores in infrared dark regions.

An interesting topic is the scale below which the nonthermal motion deviates from a continuous power law. As revealed in Section 3.2.1, the JCMT VDF of N6334I(N) follows the same power-law relation as the NANTEN2 VDF of the cloud (see Figure 1), while the JCMT VDF of N6334I is higher than this power law. This suggests that the nonthermal motions in some star formation regions have already been increased at clump-tocore scales. Below ~ 0.1 pc, all the VDFs are much higher than the fitted power law, suggesting a significant increase of nonthermal motions at subcore scales. On the other hand, we cannot rule out the possibility that the velocity statistics in lowdensity regions without star formation activities could still follow the large-scale power-law relation even at subcore scales. Thus, we conservatively conclude that, with the given data, we cannot identify a specific scale below which the velocity statistics deviate from a power-law relation.

4.2. Turbulent Motions in Massive Star Formation Regions

Nondriven supersonic turbulence decays quickly, thus inputs of energy must exist to maintain the turbulence within starforming molecular clouds (Mac Low & Klessen 2004). It has long been debated whether the turbulence is driven at a large scale (e.g., ~100 pc by supernovae; Balsara et al. 2004) and cascades to a small scale, or whether the turbulence is driven by small-scale mechanisms such as outflows (Li & Nakamura 2006; Nakamura & Li 2007) or gravitational accretion (Klessen & Hennebelle 2010). Observational studies in low-mass star formation regions usually found a power-law relation for the velocity statistics at different scales (e.g., Taurus; Yuen et al. 2022), which provides evidence for a continuous turbulent cascade. However, there is a lack of observational studies of the turbulence cascade in massive star formation regions where the gravitational effect and protostellar feedback are more significant.

In sites of massive star formation, there could be significant amounts of nonturbulent nonthermal motions (e.g., infall or rotation) in small-scale and high-density regions (Liu et al. 2021), which makes it difficult to derive pure turbulence statistics that are required for some statistical analyses (e.g., to estimate the magnetic field strength; Liu et al. 2022a). We make an attempt to remove the ordered velocity field contribution by calculating the three-point VDFs, but only the ALMA three-point VDF for N6334IV shows a plateau that is expected for pure turbulence. The plateau of the three-point ALMA VDFs for N6334IV is comparable to or higher than the NANTEN2 and JCMT VDFs at larger scales, which may provide observational evidence for turbulence driven by small-

 $[\]overline{^{16}}$ Some previous studies adopt $\mathcal{M}_s > 1$ as supersonic (e.g., Federrath et al. 2021), while other studies adopt $\mathcal{M}_s > 2$ as supersonic (e.g., Li et al. 2020). We adopt the former definition in this paper.

scale mechanisms in massive star formation regions. Such small-scale-driven turbulence could potentially reduce the star formation rate, affect the small-scale fragmentation, and shift the initial mass function to lower masses (Mathew & Federrath 2021; Hu et al. 2022).

5. Summary

We implement two-point and three-point velocity centroid structure functions on the NANTEN2 12 CO (1–0), JCMT 13 CO (3–2), SMA $\mathrm{H^{13}CO^{+}}$ (5–4), and ALMA $\mathrm{H^{13}CO^{+}}$ (1–0), NH₂D (1_{1,1}–1_{0,1}), OCS (19–18), and 13 CS (5–4) line data to study the multiscale statistics of the nonthermal motions in the massive star formation region NGC 6334. The findings are as follows:

- The combination of small-scale turbulent motions and ordered velocity fields induced by massive star formation activities increases the nonthermal motion in small-scale and high-density star formation regions, which makes the multiscale nonthermal motions in active star formation regions deviate from a continuous turbulence cascade.
- 2. The nonthermal motion revealed by the same line varies in different clumps at the same scale, which is due to the different star formation activities in these clumps. The nonthermal motions revealed by different lines show different levels in the same clump at the same scale, which is due to the different gas materials traced by these line data. These differences show that the nonthermal motions of gas materials at different densities or in different star-forming subregions do not follow a universal turbulence cascade when star formation activities are strong within the molecular cloud.
- 3. The level of nonthermal motion in the infrared dark clump N6334S is lower than that of other more evolved clumps, confirming that the nonthermal motion is increased as the clump/core evolves.
- The three-point ALMA VDFs in N6334IV show signs of pure turbulence statistics, which may provide observational evidence for small-scale-driven supersonic turbulence.
- 5. The nonthermal motion in NGC 6334 stays supersonic over several orders of magnitude.

We thank the anonymous referee for the detailed comments. We thank Dr. Doris Arzoumanian for sharing the JCMT dust continuum maps and the Herschel temperature maps. We thank Prof. Yasuo Fukui and Dr. Mikito Kohno for sharing the NANTEN2 data.

J.L. acknowledges the support from the EAO Fellowship Program under the umbrella of the East Asia Core Observatories Association. K.Q. is supported by National Key R&D Program of China grant No. 2022YFA1603100. K.Q. acknowledges the support from National Natural Science Foundation of China (NSFC) through grant Nos. U1731237, 11590781, and 11629302. H.B.L. is supported by the Ministry of Science and Technology (MoST) of Taiwan (grant Nos. 108-2112-M-001-002-MY3, 108-2923-M-001-006-MY3, 111-2112-M-001-089-MY3). Z.Y.L. is supported in part by NSF AST-1815784 and NASA 20NSSC18K1095. This work was also partially supported by the program Unidad de Excelencia María de Maeztu CEX2020-001058-M. J.M.G. also acknowledges support by the grant PID2020-117710GB-I00 (MCI-AEI-FEDER, UE).

This paper makes use of the following ALMA data: ADS/JAO.ALMA#2017.1.00793.S and ADS/JAO. ALMA#2016.1.00951.S. ALMA is a partnership of the ESO (representing its member states), NSF (USA), and NINS (Japan), together with NRC (Canada), MOST and ASIAA (Taiwan), and KASI (Republic of Korea), in cooperation with the Republic of Chile. The Joint ALMA Observatory is operated by ESO, AUI/NRAO, and NAOJ. The National Radio Astronomy Observatory is a facility of the National Science Foundation operated under cooperative agreement by Associated Universities, Inc. The JCMT is operated by the EAO on behalf of NAOJ, ASIAA, KASI, and CAMS as well as the National Key R&D Program of China (No. 2017YFA0402700). Additional funding support is provided by the STFC and participating universities in the UK and Canada. Additional funds for the construction of SCUBA-2 were provided by the Canada Foundation for Innovation. This work is based on observations obtained with Planck (http:// www.esa.int/Planck), an ESA science mission with instruments and contributions directly funded by ESA Member States, NASA, and Canada. The present study has also made use of NANTEN2 data. NANTEN2 is an international collaboration of 10 universities: Nagoya University, Osaka Prefecture University, University of Cologne, University of Bonn, Seoul National University, University of Chile, University of New South Wales, Macquarie University, University of Sydney, and Zurich Technical University.

Facilities: JCMT, SMA, ALMA.

Software: Astropy (Astropy Collaboration et al. 2013, 2018), Matplotlib (Hunter 2007).

Appendix Velocity Centroid Maps

Figures 4–7 present the intensity-weighted velocity centroid (i.e., moment 1) maps of the molecular lines used in our analysis.

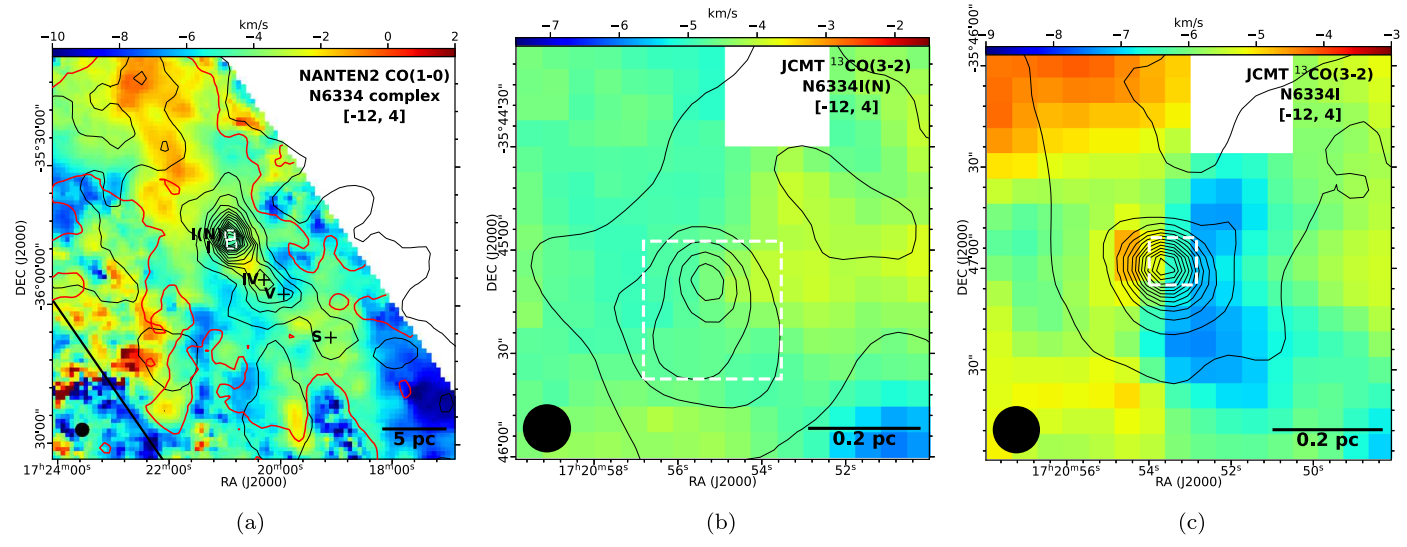


Figure 4. (a) Velocity centroid map of NANTEN2 12 CO (1–0) line emission toward the NGC 6334 complex (Fukui et al. 2018). The black contour levels correspond to the Planck 353 GHz (0.85 mm) optical depth (τ_{353}) map (Planck Collaboration et al. 2014). The contour starts at 0.0004 and continues with an interval of 0.0004. White rectangles indicate the map area of the JCMT fields in (b) and (c). Black crosses indicate the positions of N6334IV, V, and S. The red contour indicates the region within which we perform the VDF analysis. The galactic plane (black line) is indicated in the lower left corner. (b)–(c) Velocity centroid maps of JCMT 13 CO (3–2) line emission toward N6334I(N) and N6334I. The black contour levels correspond to the JCMT 0.85 mm dust continuum map (Arzoumanian et al. 2021). Contour starts at 2 Jy beam $^{-1}$ and continues with an interval of 4 Jy beam $^{-1}$. White rectangles indicate the SMA and ALMA map area toward N6334I(N) and I in Figures 6 and 7. The beam and a scale bar are indicated in the lower left and lower right corners of each panel, respectively. Panels (b) and (c) were previously shown in Liu et al. (2023) and are reproduced with permission.

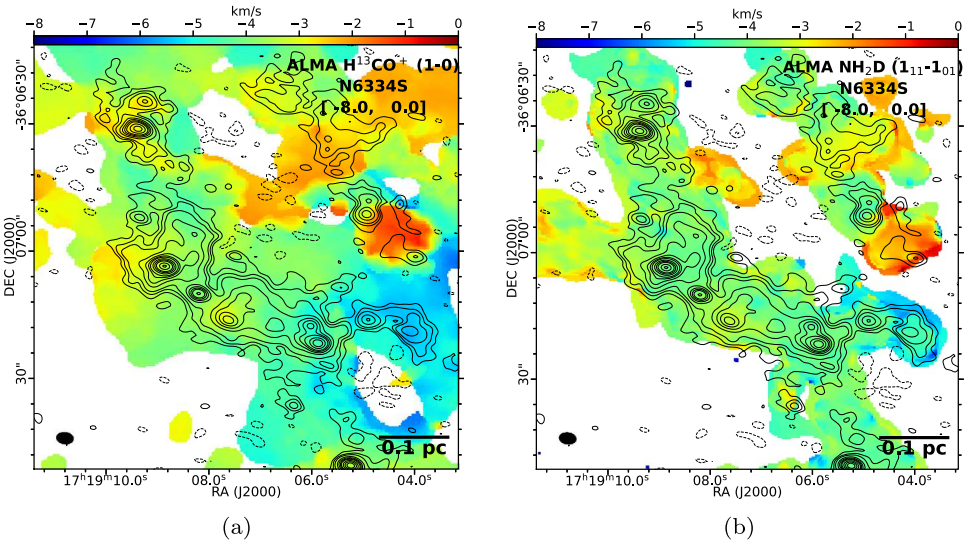


Figure 5. Velocity centroid map of ALMA (a) $\mathrm{H}^{13}\mathrm{CO}^+$ (1–0) and (b) $\mathrm{NH}_2\mathrm{D}$ (1_{1,1}–1_{0,1}) line emission toward N6334S (Li et al. 2020, 2022). The contour levels correspond to the ALMA 3 mm dust continuum map. Contour levels are $(\pm 3, 6, 10, 20, 30, 40, 50, 70, 90, 110, 150, 180, 210, 250, 290, 340, 390, 450) \times \sigma_I$, where $\sigma_I = 0.03$ mJy beam⁻¹ (Li et al. 2020) is the rms noise of the Stokes *I* map. The synthesized beam and a scale bar are indicated in the lower left and lower right corners of each panel, respectively.

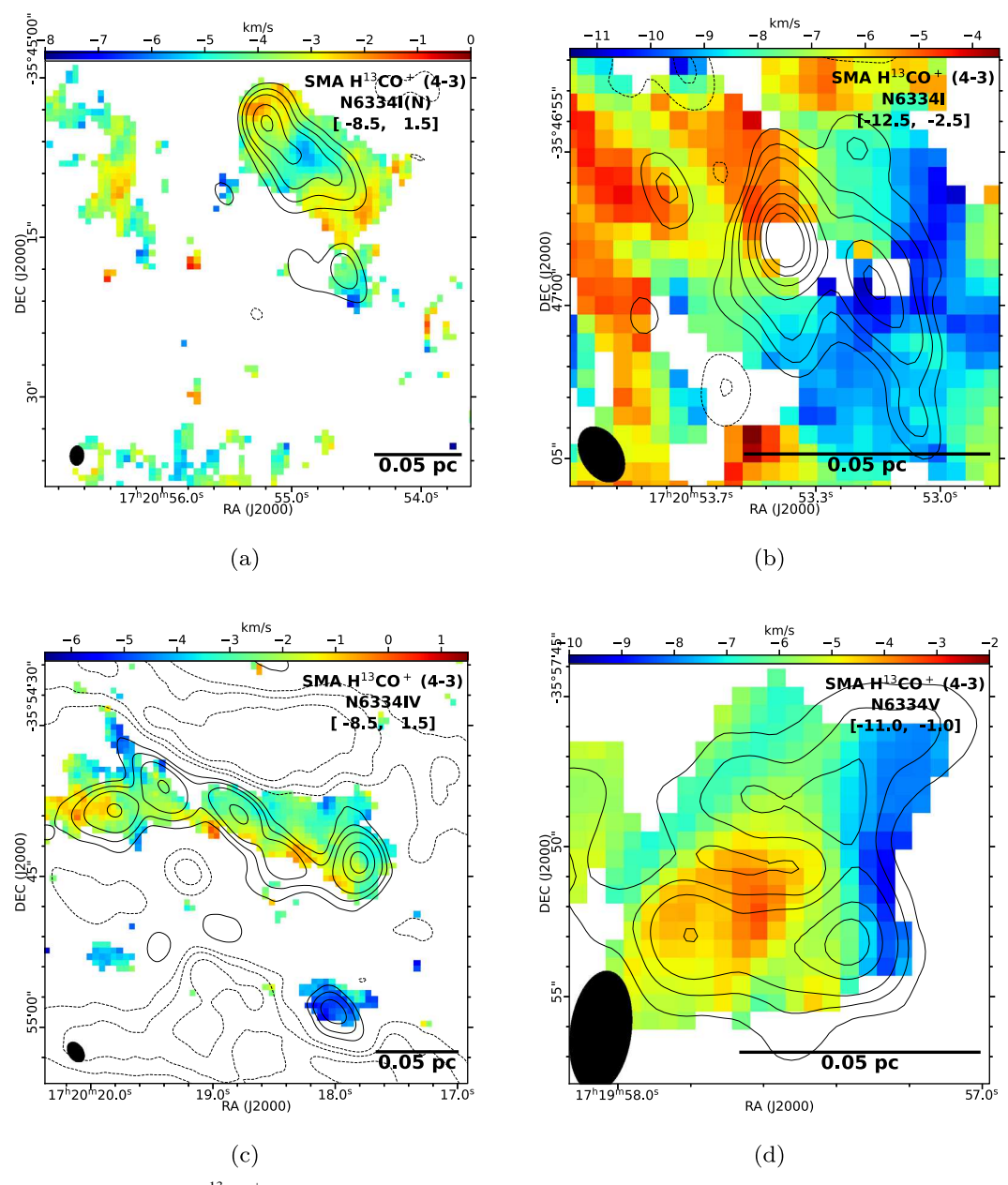


Figure 6. Velocity centroid maps of SMA H¹³CO⁺ (5–4) observations. The contour levels correspond to the SMA 0.87 mm dust continuum map (Zhang et al. 2014; Palau et al. 2021). Contour levels are (± 3 , 6, 10, 20, 30, 40, 50, 70, 90, 110, 150, 180, 210, 250, 290, 340, 390, 450) $\times \sigma_I$, where $\sigma_I = 100$, 100, 30, and 30 mJy beam⁻¹ for N6334I(N), I, IV, and V, respectively. The synthesized beam and a scale bar are indicated in the lower left and lower right corners of each panel, respectively.

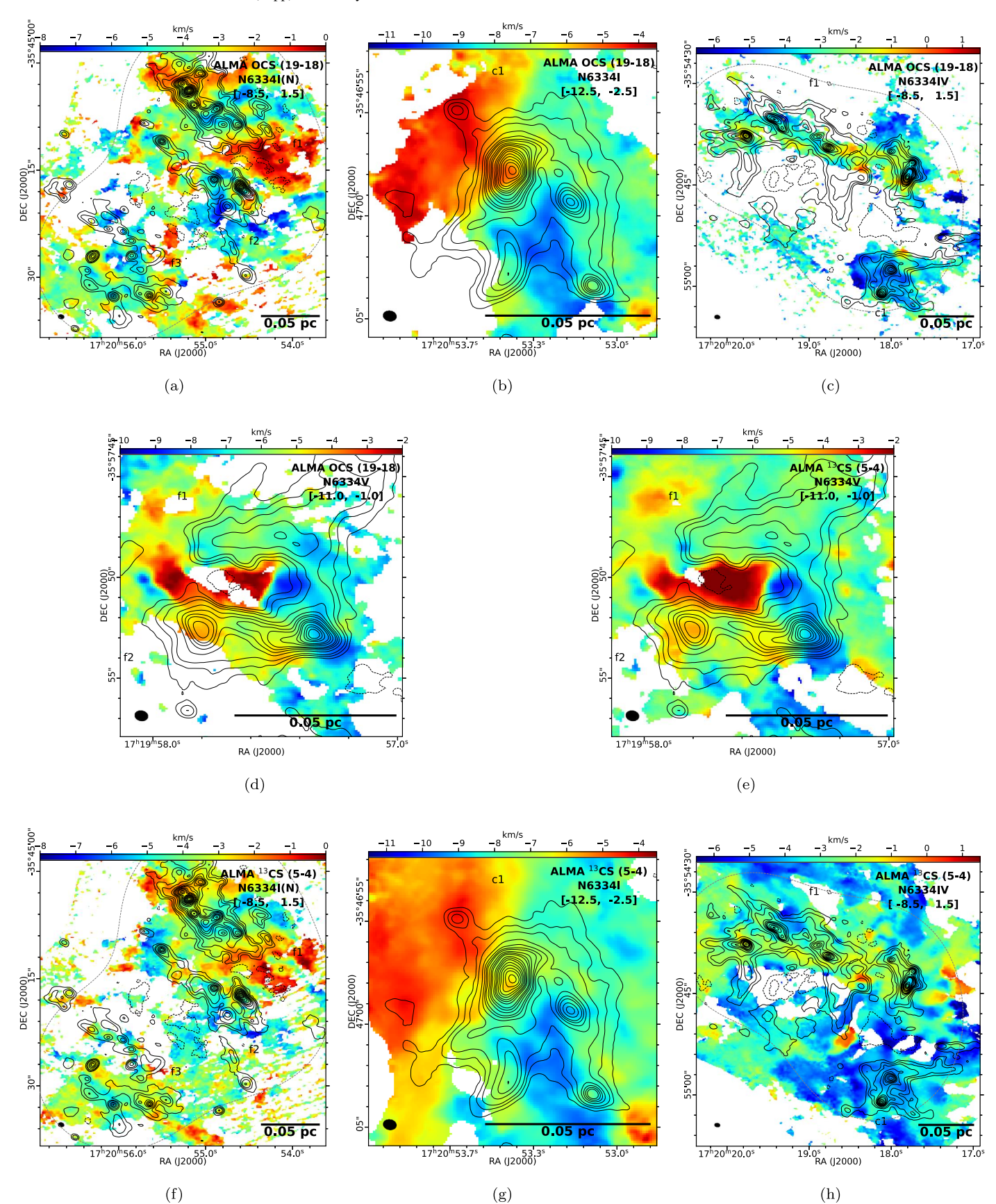


Figure 7. Velocity centroid maps of ALMA OCS ((a)–(d)) and 13 CS ((e)–(h)) observations. The contour levels correspond to the ALMA 1.3 mm dust continuum map (Liu et al. 2023). Contour levels are (± 3 , 6, 10, 20, 30, 40, 50, 70, 90, 110, 150, 180, 210, 250, 290, 340, 390, 450) $\times \sigma_I$, where $\sigma_I = 1.4$, 5.2, 1.2, and 1.0 mJy beam⁻¹ for N6334I(N), I, IV, and V, respectively. The synthesized beam and a scale bar are indicated in the lower left and lower right corners of each panel, respectively. Panels were previously shown in Liu et al. (2023) and are reproduced with permission.

ORCID iDs

```
Junhao Liu (刘峻豪) thtps://orcid.org/0000-0002-4774-2998 Qizhou Zhang https://orcid.org/0000-0003-2384-6589 Hauyu Baobab Liu https://orcid.org/0000-0003-2300-2626 Keping Qiu https://orcid.org/0000-0002-5093-5088 Shanghuo Li https://orcid.org/0000-0003-1275-5251 Zhi-Yun Li https://orcid.org/0000-0002-7402-6487 Paul T.P. Ho https://orcid.org/0000-0002-3412-4306 Josep Miquel Girart https://orcid.org/0000-0002-3829-5591 Tao-Chung Ching https://orcid.org/0000-0001-8516-2532 Huei-Ru Vivien Chen https://orcid.org/0000-0002-9774-1846
```

Shih-Ping Lai https://orcid.org/0000-0001-5522-486X Ramprasad Rao https://orcid.org/0000-0002-1407-7944 Ya-wen Tang https://orcid.org/0000-0002-0675-276X

References

```
André, P., Revéret, V., Könyves, V., et al. 2016, A&A, 592, A54
Arzoumanian, D., Furuya, R. S., Hasegawa, T., et al. 2021, A&A, 647, A78
Arzoumanian, D., Russeil, D., Zavagno, A., et al. 2022, A&A, 660, A56
Astropy Collaboration, Price-Whelan, A. M., Sipőcz, B. M., et al. 2018, AJ,
   156, 123
Astropy Collaboration, Robitaille, T. P., Tollerud, E. J., et al. 2013, A&A,
   558, A33
Balsara, D. S., Kim, J., Mac Low, M.-M., & Mathews, G. J. 2004, ApJ,
   617, 339
Buckle, J. V., Hills, R. E., Smith, H., et al. 2009, MNRAS, 399, 1026
Caselli, P., & Myers, P. C. 1995, ApJ, 446, 665
Cheung, L., Frogel, J. A., Hauser, M. G., & Gezari, D. Y. 1978, ApJL,
   226, L149
Chibueze, J. O., Omodaka, T., Handa, T., et al. 2014, ApJ, 784, 114
Cho, J. 2019, ApJ, 874, 75
Cho, J., & Yoo, H. 2016, ApJ, 821, 21
Dickman, R. L., & Kleiner, S. C. 1985, ApJ, 295, 479
Federrath, C., Klessen, R. S., Iapichino, L., & Beattie, J. R. 2021, NatAs,
Fukui, Y., Kohno, M., Yokoyama, K., et al. 2018, PASJ, 70, S41
```

Gezari, D. Y. 1982, ApJL, 259, L29

```
Goodman, A. A., Barranco, J. A., Wilner, D. J., & Heyer, M. H. 1998, ApJ,
  504, 223
Hildebrand, R. H., Kirby, L., Dotson, J. L., Houde, M., & Vaillancourt, J. E.
  2009, ApJ, 696, 567
Houde, M., Hull, C. L. H., Plambeck, R. L., Vaillancourt, J. E., &
  Hildebrand, R. H. 2016, ApJ, 820, 38
Hu, Y., Federrath, C., Xu, S., & Mathew, S. S. 2022, MNRAS, 513, 2100
Hunter, J. D. 2007, CSE, 9, 90
Juárez, C., Girart, J. M., Zamora-Avilés, M., et al. 2017, ApJ, 844, 44
Kauffmann, J., Bertoldi, F., Bourke, T. L., Evans, N. J., & Lee, C. W. 2008,
   A&A, 487, 993
Klessen, R. S., & Hennebelle, P. 2010, A&A, 520, A17
Kraemer, K. E., & Jackson, J. M. 1999, ApJS, 124, 439
Larson, R. B. 1981, MNRAS, 194, 809
Lazarian, A., Yuen, K. H., & Pogosyan, D. 2022, ApJ, 935, 77
Li, S., Sanhueza, P., Lee, C. W., et al. 2022, ApJ, 926, 165
Li, S., Zhang, Q., Liu, H. B., et al. 2020, ApJ, 896, 110
Li, Z.-Y., & Nakamura, F. 2006, ApJL, 640, L187
Liu, J., Qiu, K., & Zhang, Q. 2022a, ApJ, 925, 30
Liu, J., Zhang, Q., Commerçon, B., et al. 2021, ApJ, 919, 79
Liu, J., Zhang, Q., Koch, P. M., et al. 2023, ApJ, 945, 160
Liu, J., Zhang, Q., & Qiu, K. 2022b, FrASS, 9, 943556
Mac Low, M.-M., & Klessen, R. S. 2004, RvMP, 76, 125
Mathew, S. S., & Federrath, C. 2021, MNRAS, 507, 2448
McBreen, B., Fazio, G. G., Stier, M., & Wright, E. L. 1979, ApJL, 232, L183
Miesch, M. S., & Bally, J. 1994, ApJ, 429, 645
Muller, H. S. P., Thorwirth, S., Roth, D. A., & Winnewisser, G. 2001, A&A,
  370, L49
Myers, P. C. 1983, ApJ, 270, 105
Nakamura, F., & Li, Z.-Y. 2007, ApJ, 662, 395
Palau, A., Zhang, Q., Girart, J. M., et al. 2021, ApJ, 912, 159
Planck Collaboration, Abergel, A., Ade, P. A. R., et al. 2014, A&A, 571, A11
Sadaghiani, M., Sánchez-Monge, Á., Schilke, P., et al. 2020, A&A, 635, A2
Schöier, F. L., van der Tak, F. F. S., van Dishoeck, E. F., & Black, J. H. 2005,
   A&A, 432, 369
Solomon, P. M., Rivolo, A. R., Barrett, J., & Yahil, A. 1987, ApJ, 319, 730
Wang, Y., Zhang, Q., Pillai, T., Wyrowski, F., & Wu, Y. 2008, ApJL, 672, L33
Wu, Y. W., Sato, M., Reid, M. J., et al. 2014, A&A, 566, A17
Yuen, K. H., Ho, K. W., Law, C. Y., Chen, A., & Lazarian, A. 2022,
  arXiv:2204.13760
Zhang, Q., Hunter, T. R., & Sridharan, T. K. 1998, ApJL, 505, L151
Zhang, Q., Qiu, K., Girart, J. M., et al. 2014, ApJ, 792, 116
Zhang, Q., Wang, Y., Pillai, T., & Rathborne, J. 2009, ApJ, 696, 268
```